



Thermoelectrochemical simulations of performance and abuse in 50-Ah automotive cells



Sun Ung Kim ^{a, b, c*}, Paul Albertus ^a, David Cook ^a, Charles W. Monroe ^b, Jake Christensen ^a

^a Robert Bosch LLC, Research and Technology Center, Palo Alto, CA 94304, USA

^b Department of Chemical Engineering, University of Michigan, Ann Arbor, MI 48109, USA

^c Department of Mechanical Engineering, University of Michigan, Ann Arbor, MI 48109, USA

HIGHLIGHTS

- Dualfoil model and local energy-balance equations are implemented simultaneously.
- Temperature variation within the interior of large cells is significant.
- Risk of Li plating at low temperature is higher around the exterior of the jellyroll.
- The onset temperature that triggers thermal runaway, is lower in larger Li-ion cells.

ARTICLE INFO

Article history:

Received 8 April 2014

Received in revised form

13 June 2014

Accepted 14 June 2014

Available online 21 June 2014

Keywords:

Lithium ion battery

Dualfoil model

Mathematical modeling

Lithium plating

Thermal runaway

ABSTRACT

The performance and thermal response of large-scale GS-Yuasa LEV50 50-Ah NMC automotive battery cells were investigated via simulation. To evaluate local transient temperature distributions, the Dualfoil model was coupled to local energy-balance equations. At similar C rates the difference between maximum and minimum temperature in the LEV50 was found to be higher than that in an 18650 cell with identical chemistry. Unlike thinner prismatic lithium ion batteries, the temperature variation through the cell thickness in the large-format cell was not negligible (~5 °C at 4C discharge). Because of the non-uniform temperature distribution within the jellyroll, the risk of lithium plating at high charging rates and low ambient temperatures may be greater toward the jellyroll exterior. Simulations of thermal abuse (oven test) of the large cell showed a delayed thermal response relative to the 18650, but also indicated a lower onset temperature for thermal runaway.

© 2014 Elsevier B.V. All rights reserved.

1. Introduction

Thermal phenomena in lithium-ion batteries significantly impact both aging and safety [1,2]. Many groups have researched how ambient temperature affects capacity fade and power fade [3–11]. Higher operating temperatures have been shown to result in greater capacity fade, which has been attributed to degradation at the negative electrode [3,4] and loss of lithium inventory due to SEI rearrangement at electrode/electrolyte interfaces [5]. Thomas et al. [6] reported that the internal impedances of battery cells depend on storage temperature, suggesting that thermal phenomena may also play a part in power fade.

Most aging models (such as those by Ramadass et al. [4] and Wright et al. [11]) rely on semi-empirical equations that describe overall capacity or power fade as functions of time, state of charge (SOC), and operation or storage temperature. These phenomenological approaches neglect the effects of thermal and electrochemical inhomogeneities within the battery cell. In particular, the aging effects of temperature gradients – and consequent current-density and internal-resistance gradients – within the anode/separators/cathode ‘jellyroll’ have not been considered. Temperature can be highly non-uniform in some battery geometries, particularly during prolonged charge or discharge at high C rate [12,13]. Since temperature and the extent of cell reaction are both recognized to influence the rates of aging processes, it is possible that local thermal or electrochemical inhomogeneities could have significant global effects on aging.

Fleckenstein et al. suggested a theoretical approach to account for local inhomogeneity within the battery cell [2]. They modeled a

* Corresponding author. Lawrence Berkeley National Laboratory, 1 Cyclotron Road, MS 70R 0108B, Berkeley, CA 94720, USA. Tel.: +1 510 486 5658; fax: +1 510 486 7303.

E-mail address: sunung1979@gmail.com (S.U. Kim).

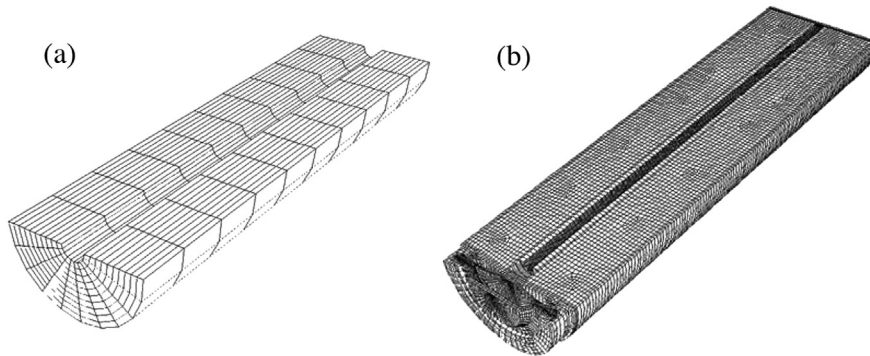


Fig. 1. Two different meshings of an 18650 (18 mm × 65 mm cylindrical) Li-ion battery cell. (a) Electrochemical mesh (b) Thermal mesh. Reproduced from reference 17 by permission of The Electrochemical Society.

32113 cylindrical cell using an equivalent-circuit-based model (ECM) [14,15] for the electrochemical response of each volume element in the battery interior. Using the local values of current from the ECMs, the Joule heating (I^2R) and local reversible heats of reaction ($IT \, dU/dT$) could be evaluated in each volume element, coupling the local ECMs to a partial differential equation describing the detailed local heat balance. Although Fleckenstein et al.'s model yields a local temperature distribution, and can match experimental data effectively, it has the same limitation as other ECMs: the resistors and capacitors involved in the electrical model do not have clear physical interpretations. Thus the values of fit parameters cannot be used to develop an understanding of the microscopic mechanisms that cause degradation.

Recently Christensen et al. introduced a different method to analyze thermal inhomogeneity in 18650 lithium-ion cells [16,17]. They suggested expanding the one-dimensional electrochemical cell-sandwich model (the standard Dualfoil model) [18–20] instead of relying on an ECM. The Dualfoil model is based on detailed models of interfacial electrochemistry and multi-phase electrochemical transport. Within Dualfoil, lithium transport in the separator and both electrodes is modeled explicitly, as are interfacial reaction kinetics and reaction thermodynamics. Typical implementations of Dualfoil assume the cell sandwich has a nearly uniform temperature, suggesting that the Biot number of the battery cell is relatively small and its internal heat conductance is relatively high [21]. The Biot number Bi is

$$Bi = \frac{hL_c}{k}, \quad (1)$$

where h is the heat-transfer coefficient between the cell and its surroundings, L_c a characteristic length (e.g., cell thickness), and k a characteristic thermal conductivity of the cell. Dualfoil receives current or voltage as input variables, and returns voltage or current (respectively), along with additional information such as SOC, extent of concentration polarization in the cell sandwich, and surface overpotentials in the anode and cathode. See [Appendix A](#) for the Dualfoil equations used in this work.

When the Biot number is high ($Bi \gg 1$), internal temperature variation is significant, and a single cell-sandwich Dualfoil model cannot accurately describe the electrochemical behavior of every layer in the jellyroll that comprises a battery cell. To address this limitation, Bosch researchers proposed several techniques to couple the Dualfoil model to a local energy-balance equation [16,17]. If Soret/Dufour diffusion is negligible, the thermal and electrochemical models are formally decoupled; the electrochemical and thermal problems can be solved sequentially at a given time step. This allows the spatial domain of the problem to be

separately meshed over different length scales appropriate to the electrochemical and thermal problems. (The characteristic length for mass-transfer processes is the thickness of a single layer of the jellyroll, whereas the characteristic length scale for heat transfer is a dimension of the whole cell.) The entire battery was divided into a number of electrochemical volume elements, each of which was modeled by a one-dimensional cell-sandwich model essentially identical to the original implementation of Dualfoil. At the same time, the battery cell was divided into a set of thermal volume elements, which do not necessarily coincide with the electrochemical elements. Exemplary thermal and electrochemical meshings used for the past simulations by Christensen et al. [16,17] are reprinted in [Fig. 1](#). Although the thermal problem does not in principle require a very dense mesh, fine thermal meshings are still necessary to help to illustrate the temperature variation inside the jellyroll. Unlike Dualfoil, which is stiff and computationally expensive, the thermal problem only requires solving a single second-order linear differential equation, and therefore can be solved extremely rapidly over a fine mesh.

To implement simulations, each electrochemical volume element is taken to exist at the average temperature of the thermal elements it contains. The solution process is as follows: first, the electrochemical problem is solved throughout the cell; once convergence is reached, the heat-generation rate in each electrochemical element is passed to the thermal model; the temperature in each thermal element is subsequently updated by solving the energy balance, and the updated temperatures are returned to the electrochemical elements for the next time step [17].

The desire to observe local variation of electrochemical variables such as overpotential places an upper bound on the electrochemical mesh size. On the other hand, the computational expense places a lower bound on the mesh size. Thus there should be an optimal electrochemical mesh size that describes local electrochemical transport sufficiently accurately, contains cells across which temperature gradients are minimal, and is computationally efficient.

This work expands Christensen et al.'s method to larger lithium-ion batteries, and provides a tool for assessing battery safety. Although state-of-health effects are beyond the scope of this paper, the model also provides a tool for simulating cell aging, including nonuniformity due to thermal variation, as has been presented for 18650 cells [22]. Large-capacity lithium-ion cells have received significant interest in the past several years because of the high energy demands set by a variety of applications, including transportation [23]. In the past, electric-vehicle batteries have comprised packs of 18650 cells (2–3 Ah capacity per cell) [24]. The market is moving to larger capacity cells such as the LEV50 (50 Ah per cell); their surface-to-volume ratios are lower, reducing packaging cost. The total energy density of battery systems based on

large-capacity cells (including the battery casing itself, as well as peripherals such as mounting brackets, exhaust-gas manifolds, and control circuitry) can be higher, saving space. But the same reductions in surface-to-volume ratio that lower cost and raise energy density make thermal management more difficult, calling for a better understanding of coupled electrochemical/thermal processes.

2. Model description

A representation of the GS Yuasa LEV50 cell geometry was created, using details of the casing configuration from the company website [25]. The battery geometry used for the present work is shown in Fig. 2, which also illustrates the thermal mesh. Information about the battery interior was unavailable (it is intellectual property of GS Yuasa Inc.); therefore, plausible assumptions were made about the geometric configuration and materials used within the cell. The mesh was built using Gambit (Ansys Inc.) [26]. The whole thermal mesh is composed of hexahedral volume elements (1 mm^3 on average), for a total of 678,862. In contrast, the electrochemical model used to describe the jellyroll within the cell comprises larger (230 mm^3 on average) volume elements, for a total of 3,375 ($= 15^3$); the electrochemical volume elements are arbitrary shapes of various size bounded by parallelepipeds, delineated by 15 mesh points each in the x , y , and z directions of the jellyroll. Most of the electrochemical elements are parallelepipeds; however, some of the elements located at the jellyroll corners have a curved geometry. The tabs and uncoated current-collector regions that connect the jellyroll to the cell terminals do not require the electrochemical mesh because there is no electrochemical reaction or mass diffusion there. For details about the procedures used to map meshes and transfer temperatures and electrochemical states between electrochemical and thermal simulation steps, see references 16 and 17. The key difference in this work is that, since the battery geometry is prismatic, the code mapping between electrochemical cells and thermal cells [16,17] was rewritten to use a three-dimensional Cartesian coordinate frame, rather than cylindrical coordinates.

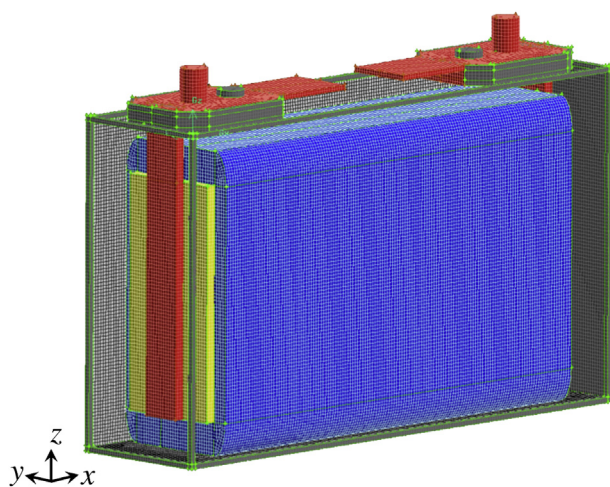


Fig. 2. Thermal mesh of the GS Yuasa LEV50 cell geometry. The exterior casing is 171 mm L \times 44 mm W \times 115 mm H. The blue domain represents the jellyroll; yellow represents uncoated regions of the copper current collector, and red, the nickel tabs and terminals. An additional aluminum current collector on the right side of the battery cell is obscured by the jellyroll. An extremely low-pressure gas (or vacuum) was assumed to occupy the space between the jellyroll and the casing. (For interpretation of the references to color in this figure legend, the reader is referred to the web version of this article.)

Different domains within the cell were modeled with different heat-generation terms in the local energy balance. For the jellyroll, the following sources of electrochemical heat generation were included: irreversible Joule heating from the internal impedances of the electrodes and separator, as well as reversible heating from the entropy change with respect to charge state in each electrode material. For the current collectors, tabs, and terminals, only irreversible Joule heating was included. Evaluating the Joule heating, the volumetric current density was assumed to be uniform in the tabs, and to be linearly distributed in the z direction within the current collectors (the current density is zero at the bottom of the current collector, and is the same as the total current density of the tabs at the top of the current collector). A jellyroll is not employed in the evaluation in these regions. No heat generation terms were included in the stainless-steel housing domain, which was assumed to be electrically isolated from the jellyroll and tabs.

The thermal properties used to parameterize different domains of the cell are summarized in Table 1. The Fluent material database provided property values for steel, nickel, copper, and aluminum, taken from a variety of sources [27–29]. Properties of the jellyroll were also taken from the literature [30].

A jellyroll generally consists of a wound electrode stack. In the case of cylindrical cells, the jellyroll is macroscopically modeled as a homogenous annulus with anisotropic thermal conductivity because heat travels much faster through the current collectors than through the plane of the separator – exhibiting low radial, and high axial and azimuthal, thermal conductivities [2,17]. Although the GS Yuasa cell is also wound, the configuration of the winding makes it better considered as a multilayer sandwich over the majority of its volume. Fig. 3(a) is taken from an article [31], which illustrates the spiral-winding configuration and suggests how anisotropic thermal conductivity should be taken into account in a macro-homogeneous thermal model of the jellyroll. The heat transfer is anisotropic because the current-collector layers within the jellyroll have much higher thermal diffusivity than the separator. Therefore, on a layer of the jellyroll normal to the y direction in Fig. 2 and near its geometric center on the xz plane, heat conduction in the y direction will be much slower than it is in the xz plane.

Note that Table 1 shows that two different thermal conductivity values were used in the z direction for the jellyroll, because of the complexity added by the jellyroll winding. Fig. 3(a) shows that at the top and bottom of the jellyroll, there are small domains where the layers predominantly occupy the xy plane, *i.e.*, where the separator is normal to z . In these domains the thermal conductivity in the z direction was reduced to the same value in the y direction. A user-defined function was written and included in the Fluent code to implement this property variation. Note that the thermal conductivity tensor was assumed to be diagonal for simplicity.

Fig. 4 shows local temperature distributions that arise within the LEV50 after 550 s of discharge at a 4C rate (200 A), assuming a

Table 1

Assumed thermal properties of the GS-Yuasa LEV50 [27–30]. Anisotropic thermal conductivities are included in the jellyroll [2] (see Fig. 3(b) for more information about the thermal conductivities in the z direction).

Volume	Material	$k (\text{W m}^{-1} \text{K}^{-1})$	$\rho (\text{kg m}^{-3})$	$c_p (\text{J kg}^{-1} \text{K}^{-1})$
Jellyroll	Multiple	$x: 28$ $y: 1.5$ $z: 1.5, 28$	2708.2	781.38
Housing	Steel	16.27	8030	502.48
Tabs & terminals	Nickel	91.74	8900	460.6
Current collectors	Copper	387.6	8978	381
	Aluminum	202.4	2719	871

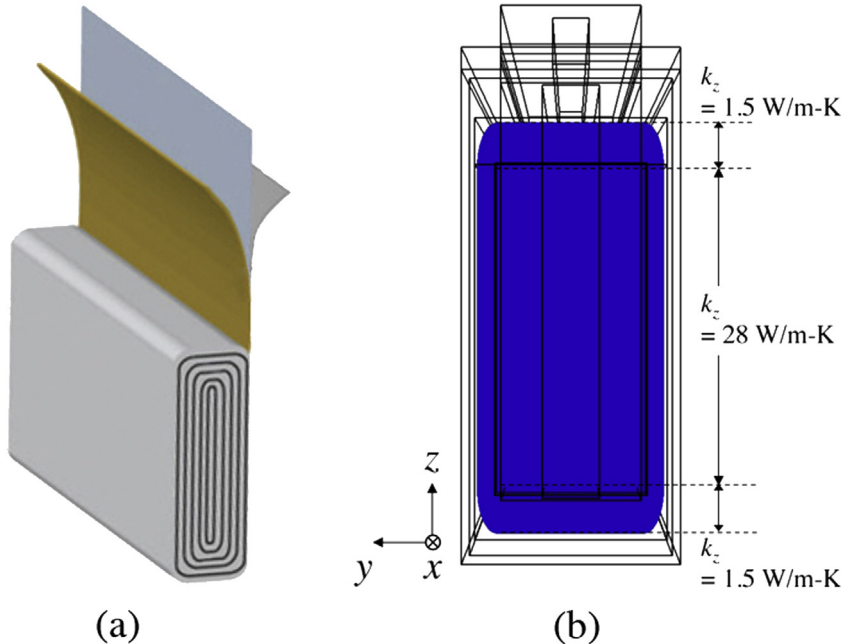


Fig. 3. (a) An exemplary picture of jellyroll from a prismatic battery (reproduced from reference 31 by permission of Elsevier); (b) distribution of non-uniform z direction thermal conductivity, implemented in the Fluent program.

thermal conductivity in the z direction that is (a) nonuniform and (b) uniform. (In the latter case, a uniformly high conductivity, $k_z = 28 \text{ W m}^{-1} \text{ K}^{-1}$, was used.) The battery was taken to be initially thermally equilibrated at an ambient temperature of 298 K; a heat-transfer coefficient of $h = 40 \text{ W m}^{-2} \text{ K}^{-1}$, corresponding to forced convection, was used on the outer boundary of the stainless-steel housing; the bottom of the housing was taken to be thermally insulated, as it may be in an environmental chamber during single-cell testing.

Fig. 4(c) shows the centerline temperature in the z direction; the base of the centerline is located at the body-center point of the battery bottom plate (in the xy plane). One can see that lower thermal conductivity in the z direction at the top and bottom of the jellyroll leads to significant differences in the temperature distribution in the lower portion of the jellyroll. Both of the cases have a thermally insulated boundary at the bottom, but the lower thermal conductivity results in a greater temperature gradient in the top and bottom region of the jellyroll. Lower thermal conductivity results in higher overall temperature and greater local temperature gradients. These facts are important because the local temperature and its gradients are critical to battery safety and cycle life.

3. Performance results

3.1. Thermal boundary conditions

The developed simulation tool was used to test the impact of local internal temperature on battery performance. First, the effects of different thermal boundary conditions on the internal temperature distribution within the battery cell were assessed. Four different boundary conditions were simulated with a 4C discharge current (200 A) and initial uniform temperature of 298 K. (An insulating boundary condition at the bottom face of the battery housing was used in all cases.) Fig. 5(a) shows four different temperature distributions at $t = 510$ s that arise from different thermal boundary conditions on the battery housing and terminals. Cases 1 and 2 in Fig. 5(a) use natural-convection boundary conditions on

the battery housing, with $h = 8 \text{ W m}^{-2} \text{ K}^{-1}$; cases 3 and 4 use forced convection there, with $h = 100 \text{ W m}^{-2} \text{ K}^{-1}$; cases 1 and 3 use identical convective boundary conditions at the surface of the terminals; cases 2 and 4 assume isothermal conditions (298 K) at the surfaces of the terminals. Conditions of constant tab temperature were tested because in testing and in application, batteries are usually connected to large thermal masses maintained at ambient temperature (such as cabling or other power electronics), to which heat is readily conducted through electrically conductive materials. The actual heat flux at the terminals should in general lie between those corresponding to the convective and isothermal boundary conditions.

A more detailed comparison can be made using Fig. 5(a), which compares centerline temperature distributions from Fig. 5(a). In line with physical expectations, natural convection (cases 1 and 2) results in higher peak and average temperature, whereas forced convection (cases 3 and 4) results in greater temperature gradients. In cases 2 and 4, the forced low temperature at the tabs induces much higher heat fluxes there, lowering the overall temperature relative to cases 1 and 3. As expected from the relative surface areas, the convective cooling conditions across the two largest faces of the cell are more influential than the terminal thermal boundary conditions. Natural convection results in a higher but more uniform temperature distribution through the thickness of the cell, as is expected due to the lower Biot number. We have shown previously in simulations that average temperature is a stronger determinant of cell aging than is temperature uniformity [22]; hence, a thermal management system with forced convection is expected to improve battery lifetime.

3.2. Local distribution of temperature

The evolution of temperature profiles within the jellyroll is illustrated in Fig. 6, which shows several different instants after the start of a 4C (200 A) discharge. The simulation was stopped at $t = 556$ s, when a cell voltage of 3.0 V was reached. Owing to the convection from the cell exterior, the temperature at the central

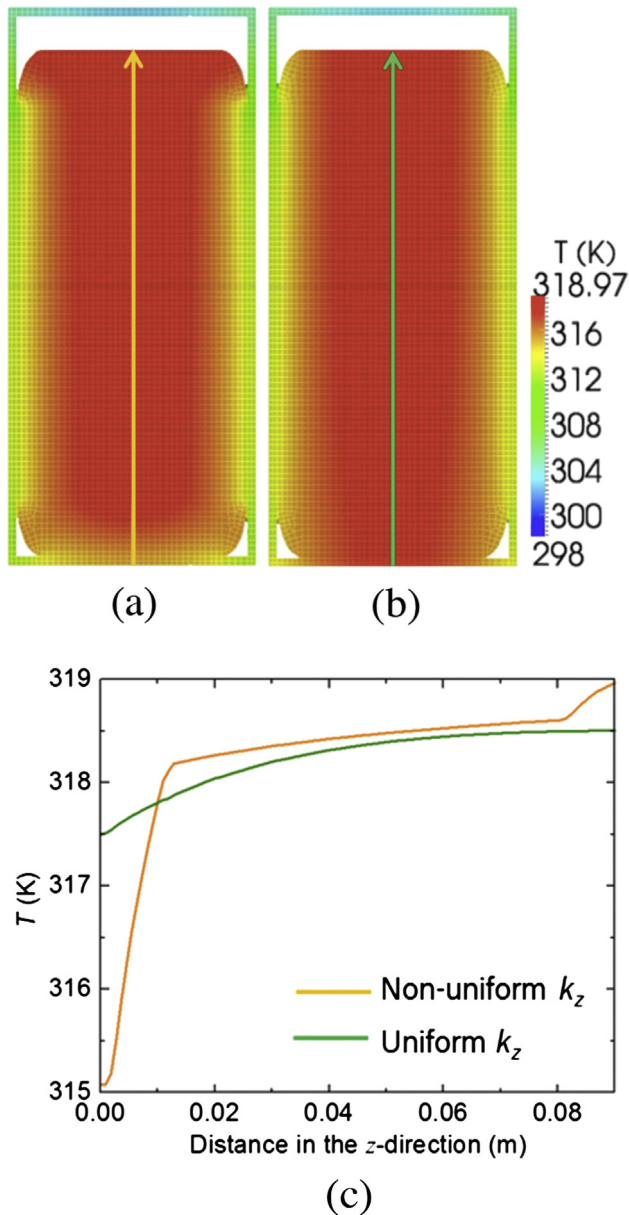


Fig. 4. Low thermal conductivity at the top and bottom of the jellyroll affects the local temperature distribution: (a) anisotropic thermal conductivity of Fig. 3(b), (b) uniformly high thermal conductivity in the z direction, and (c) comparison of the temperature along the arrow in (a) and (b).

part of the jellyroll was always higher than its exterior surfaces. Fig. 6(d) shows that the average temperature is closer to the maximum than to the minimum, as expected from the roughly parabolic shape of the distribution through the battery cross section in the y direction. Thus most parts of the battery have a higher temperature than the average, suggesting that rates of thermally activated degradation will be higher than predicted by a model based on average cell temperature.

As time elapsed, the relative difference between maximum and minimum temperature in the jellyroll rose, eventually reaching about 9 °C at the end of the 4C-discharge simulation. This temperature difference is much greater than that observed in 18650 cells, which have much larger surface-to-volume ratios. Thermal phenomena may consequently lead to much more significant impacts on aging, safety, and overpotential distribution in large-format batteries.

While most previous thermal modeling [12,13,32,33] has neglected the temperature distribution through the cell thickness (y direction in Fig. 2), the present simulations indicate that temperature variation in this direction is significant because of the large Biot number associated with large-format cells. Detailed 3-D modeling of the energy balance may be necessary to make accurate predictions about large-format battery performance.

4. Implications for battery safety

Local temperature and current distributions can provide information about failure mechanisms in automotive battery systems. Two key failure mechanisms, lithium-metal plating and thermal runaway, are discussed in this section. Tests pertinent to these safety issues were performed using the developed simulation tool.

4.1. The lithium plating side reaction

During charging, lithium ions ideally intercalate into the porous graphite negative electrode (colloquially called the ‘anode’, although it acts as a cathode during recharge). If the surface overpotential at the negative electrode is below zero, it becomes thermodynamically favorable to plate lithium metal on the solid surface. As lithium plating continues, dendrites can form; the dendrite propagation can cause internal short circuits and consequent catastrophic battery failure. Even when there is insufficient dendritic growth to short the cell, high-surface area lithium deposits in contact with organic electrolyte are highly reactive and may accelerate the onset of thermal runaway under abusive conditions. When a lithium-ion battery is exposed to a high enough temperature, the heating triggers a spontaneous exothermic chemical reaction, in a process typically called ‘thermal runaway’ [1]. A detailed mechanism of thermal runaway is provided in the next subsection. The process of lithium plating on a porous graphite negative electrode has been imaged *in situ* by Harris et al. [34].

To examine lithium plating, a charge step at 4C from an initial state of 50% SOC was simulated with forced-thermal-convection boundary conditions on the battery housing and tabs, at four different ambient temperatures. Charging was stopped when the battery voltage reached a cutoff of 4.35 V. Fig. 7(a) presents typical data at 20 °C, which show the outer area of the jellyroll to have the most negative overpotential (the highest driving force for Li plating), suggesting that more lithium plating is likely to occur there. Negative-electrode surface overpotentials that occur during 4C charging in ambient temperatures of 10 °C, 15 °C, 20 °C, and 25 °C are shown in Fig. 7(b). Lower ambient temperature appears to increase the propensity for lithium plating at high current. All in all, lithium plating is more likely at the outer surface of the jellyroll, and could be severe in low-temperature ambients.

4.2. Thermal runaway

High ambient temperatures also lead to safety concerns. Hatchard et al. modeled the thermal runaway of 18650 LiCoO₂/graphite cells using a theoretical description of a proposed SEI decomposition reaction [35,36]. The reaction was hypothesized to proceed *via* several steps: first, in the range 90–120 °C, the metastable SEI phase reorganizes into a stable SEI film; second, around 150 °C, anode-intercalated lithium reacts with the electrolyte to thicken the stable SEI film; finally, the LiCoO₂ cathode evolves oxygen, which rapidly reacts with the electrolyte, above ~175 °C. These reaction steps are highly exothermic and accompanied by a significant release of heat. To account for thermal runaway, heat generation terms were added to the energy balance that describe the reactions in Hatchard et al.’s thermal abuse mechanism. (See Appendix B and Table B1 for

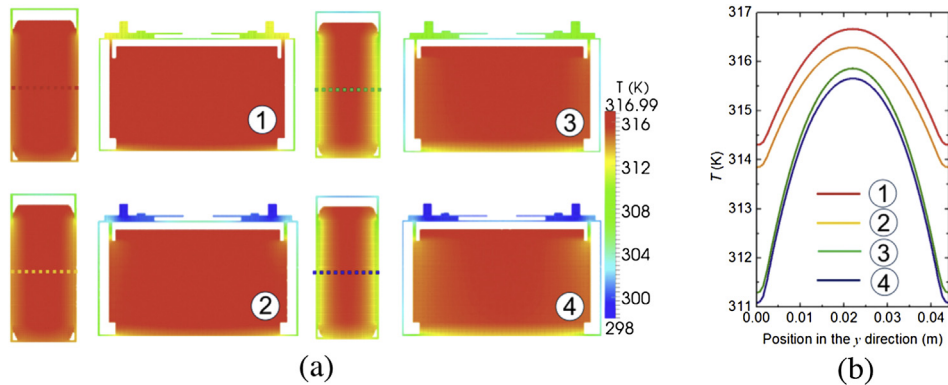


Fig. 5. Effects of different boundary conditions on the local temperature distribution: (a) front and side views of four different cases, (b) temperature distributions along the centerline shown in Fig. 5(a). Cases 1 and 2 use natural-convection boundary conditions on the battery housing, with $h = 8 \text{ W m}^{-2} \text{ K}^{-1}$; cases 3 and 4 use forced convection there, with $h = 40 \text{ W m}^{-2} \text{ K}^{-1}$; cases 1 and 3 use identical convective boundary conditions at the surface of the terminals; cases 2 and 4 assume isothermal conditions (298 K) at the surfaces of the terminals. The cells are discharged at 4C ($t = 510 \text{ s}$).

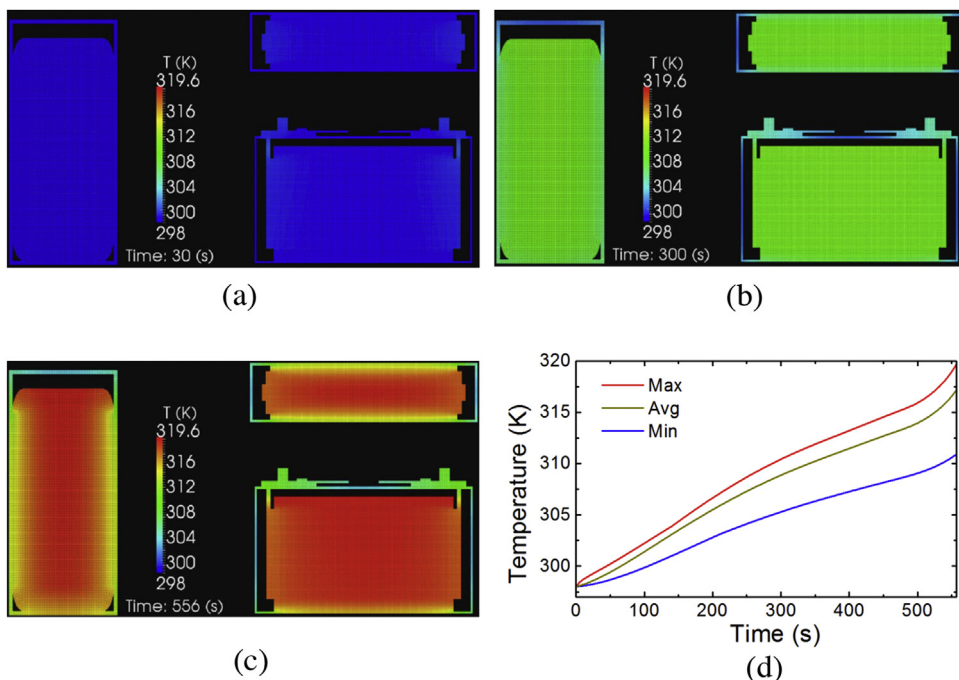


Fig. 6. Non-uniform temperature distribution at three different instants during a discharge at 4C (same conditions as case 3 in Fig. 5), started in equilibrium with the ambient temperature: (a) 30 s, (b) 300 s, and (c) 556 s; (d) maximum, minimum, and volume-average temperature of the jellyroll throughout the discharge duration.

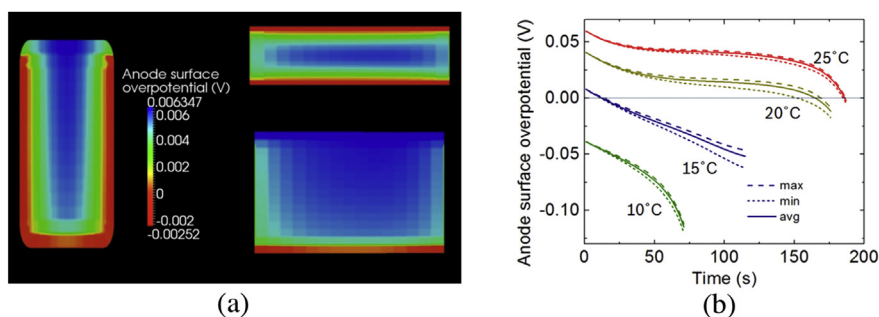


Fig. 7. The local distribution of anodic surface overpotential. (a) A case of 4C recharge in a 20 °C ambient shows that the outer area of the jellyroll has more Li plating after 160 s. (b) Anode surface overpotentials with different ambient and initial temperatures demonstrate that lower ambient temperatures result in more Li plating.

the model equations and parameters.) Here we apply the thermal abuse mechanism Hatchard et al. reported for the LiCoO₂/graphite chemistry [35]. Although the large-format cell chemistry of interest here is different (NMC cathode), the LiCoO₂-based thermal abuse simulations still help to illustrate characteristic differences between large-format and consumer-sized cells.

Fig. 8 shows simulated thermal runaway tests for 18650 and LEV50 cells at four different ambient temperatures from 140 °C to 155 °C. In each simulation, the battery was initially equilibrated at 25 °C and forced-convection boundary conditions were applied. As expected, in Fig. 8(a), one can see that an ambient temperature of 140 °C is too low to trigger the exothermic reaction; higher temperatures lead to faster thermal runaway with higher peak temperatures. More importantly, the large-format cell undergoes thermal runaway at a lower oven temperature and has a higher peak temperature, but the time to reach the peak temperature is longer. This is in accord with physical intuition; the smaller surface-to-volume ratio of the large cell implies slower heating to the oven temperature, but also results in a greater imbalance between internal heat generation and heat removal once the exothermic thermal abuse reactions are activated.

5. Conclusions

A simulation tool introduced previously [17] was applied to investigate the impact of cell format on battery performance and thermal response for a large-scale commercial automotive battery (the GS-Yuasa LEV50 50 Ah NMC cell). For simulations, the standard Dualfoil model was coupled to a local energy balance to get transient temperature distributions within the battery. In contrast to

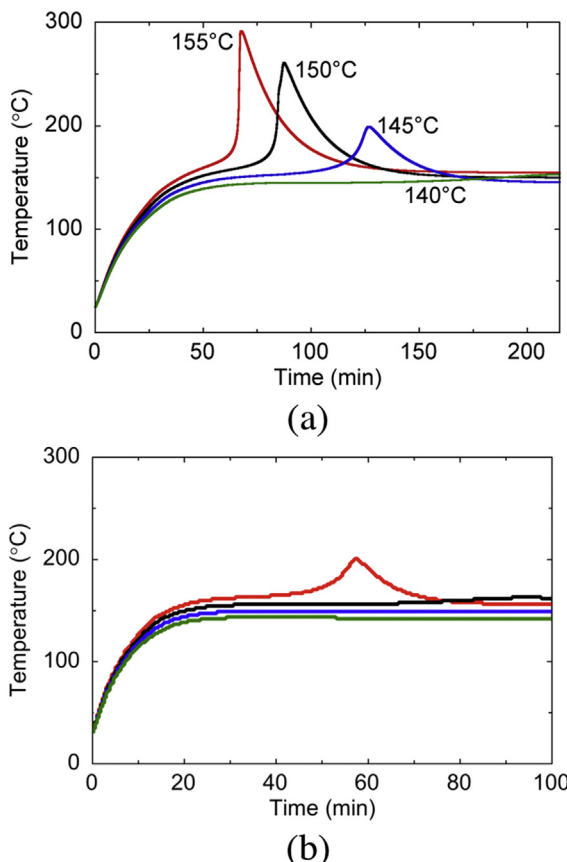


Fig. 8. The thermal runaway simulations (oven test) at four different ambient temperatures in two batteries: (a) 50-Ah automotive cell (b) 18650 cell.

simulations of 18650 cells, three-dimensional simulations were found to be necessary for the large-format cell because of its large size and Biot number, as well as its complex geometry. Anisotropic heat conduction in the jellyroll was also taken into account, and found to have an impact on temperature distributions.

Transient solutions were obtained describing the local distributions of temperature and current density in the large-format cells. The local temperature difference at 4C was as high as 10 °C, larger than 18650 cells operated at a similar C rate. Because of a high Biot number, the temperature variation within the jellyroll is significant in the large-scale battery.

Simulations of lithium plating during fast charging and thermal runaway at elevated temperature, both of which relate to cell safety, were performed. At high charging rates (4C), more lithium plating is expected around the outer surface of the jellyroll; this nonuniformity can be more significant at low ambient temperatures.

Oven tests of both an 18650 cell and the LEV50 cell were simulated to estimate the influence of battery size on thermal runaway. When subjected to the same initial and ambient temperatures, thermal runaway of the larger cell was found to occur more slowly, but the critical ambient temperature for thermal runaway was several degrees lower. Both of these observations are consequences of the lower surface-to-volume ratio of the large-format cell in comparison to the 18650. Nonuniform degradation induced by the temperature distribution within the jellyroll will be the subject of future work.

Appendix A. Dualfoil: the set of equations and electrochemical properties used [16–20].

Mass balance: ion transport in the electrolyte

$$\epsilon \frac{\partial c_{\text{elyte}}}{\partial t} = \nabla \cdot \left[D_{\text{eff}} \nabla c_{\text{elyte}} + \frac{i_{\text{elyte}}(1 - t_+)}{F} \right]$$

Mass balance: Li transport in the active material

$$\frac{\partial c_s}{\partial t} = \nabla \cdot (D_s \nabla c_s)$$

Charge balance: distribution of ionic/electronic current

$$a j_{n,k} = \frac{-s_k \nabla \cdot i_{\text{elyte}}}{nF}$$

Ohm's law: ionic current in the electrolyte

$$i_{\text{elyte}} = -k \nabla \phi_{\text{elyte}} + 2 \frac{kRT}{F} (1 - t_+) \left(1 + \frac{\partial \ln f_{+-}}{\partial \ln c_{\text{elyte}}} \right) \nabla \ln c_{\text{elyte}}$$

Ohm's law: electric current in the solid matrix

$$I - i_{\text{elyte}} = -\sigma \nabla \phi_s$$

Butler–Volmer equation: electrochemical reaction rates

$$j_{n,k} = \frac{-s_k}{nF} i_{0,k} \left[\exp\left(\frac{\alpha_a F}{RT} \eta_s\right) - \exp\left(\frac{\alpha_c F}{RT} \eta_s\right) \right]$$

Tafel equation: cathodic side reaction rate

$$i_{\text{side}} = -i_0 \exp\left(-\frac{\alpha_c F}{RT} \eta_s\right)$$

Heat generation rate: based on local reaction rate, SOC

$$\dot{q} = - \int_v \sum_k a i_{n,k} U_{H,k} dv - IV$$

Electrochemical properties, used in the model, are demonstrated in Table A1. An Arrhenius temperature dependence was adopted for kinetic and transport properties. The table includes the activation energies, E , normalized by the gas constant, R , in units of temperature (K). Christensen et al. measured some of these values using separately prepared coin cells for half-cell electrochemical measurements; other values are drawn from the literature or are fitted. See Ref. [17] for more information on the parameter values.

Table A1
Cell sandwich parameters used for all charge/discharge simulations.

	Li _x C ₆	Li _y Ni _{0.33} Mn _{0.33} Co _{0.33} O ₂
<i>Design-adjustable parameters</i>		
Electrode thickness, μm	53	59
Volume fraction electrolyte	0.38	0.37
Volume fraction inert filler	0.12	0.1
<i>Electrode parameters</i>		
Solid-phase diffusion coefficient, $\text{m}^2 \text{s}^{-1}$	9.88×10^{-15}	6.0×10^{-15}
Film resistance, Ωm^2	0.002	0.001
D50 particle radius, μm	11	5.5
Reaction rate constant, $\text{mol m}^{-2} \text{s}^{-1}$	4.4×10^{-10}	1.0×10^{-9}
Density, g cm^{-3}	2.11	4.80
Specific capacity, mAh g^{-1}	372	278
Matrix conductivity, S m^{-1}	100	100
Initial values of x and y	0.77	0.378
<i>Cell sandwich parameters</i>		
Separator thickness, μm	20	
Separator porosity (Celgard 2400)	0.52	
Salt concentration (LiPF ₆ in EC/DEC), M	1.0	
<i>Activation energies (E/R)</i>		
Solid state diffusion, K	3500	2300
Electrolyte conduction, K	4000	
Electrolyte diffusion, K	4000	
Insertion kinetics, K	14,000	15,000
Film resistance, K	4400	1300

Appendix B. Thermal abuse model: the set of equations and parameters used[35].

Heat balance:

$$\frac{\partial(\rho \hat{C}_p T)}{\partial t} = -\nabla \cdot (k \nabla T) + S_{\text{abuse}}$$

$$S_{\text{abuse}} = S_{\text{SEI}} + S_{\text{ne}} + S_{\text{pe}}$$

SEI Reaction (metastable to stable SEI):

$$\Delta x_f = -A_1 x_f^n \exp\left(\frac{-E_1}{k_B T}\right) \Delta t$$

Here x_f is the amount of lithium-containing metastable species in SEI.

Negative solvent reaction:

$$\Delta x_i = -A_2 x_i \exp\left(\frac{-\zeta}{\zeta_0}\right) \exp\left(\frac{-E_2}{k_B T}\right) \Delta t$$

$$\Delta \zeta = A_2 x_i \exp\left(\frac{-\zeta}{\zeta_0}\right) \exp\left(\frac{-E_2}{k_B T}\right) \Delta t$$

Here x_i is the amount of lithium intercalated within carbon, and ζ is the dimensionless measure of SEI thickness.

Positive solvent reaction:

$$\Delta \alpha = A \exp\left(\frac{-E_a}{k_B T}\right) \alpha^m (1 - \alpha)^n [-\ln(1 - \alpha)]^p \Delta t$$

Here $\Delta \alpha$ is the fractional degree of conversion of cathode.

Heat generation:

$$S_{\text{pe}} = H W A \exp\left(\frac{-E_a}{k_B T}\right) \alpha^m (1 - \alpha)^n [-\ln(1 - \alpha)]^p$$

$$S_{\text{SEI}} + S_{\text{ne}} = H_1 W_1 A_1 x_f^n \exp\left(\frac{-E_1}{k_B T}\right) + H_2 W_2 A_2 x_i \exp\left(\frac{-\zeta}{\zeta_0}\right) \exp\left(\frac{-E_2}{k_B T}\right)$$

Table B1 shows initial conditions of the simulation and key properties in the model. Table B1 also includes the activation energies, E_i , which have units of eV; therefore, those are normalized by the Boltzmann constant, k_B , to have consistent units of temperature (K). See Ref. [35] for the details and complete set of parameters.

Table B1
Initial condition and parameters used for all abuse simulations.

	Values
<i>Initial dimensionless concentrations</i>	
Solvent	1.0
SEI	0.15
SEI thickness, z_0	0.033
Negative electrode	0.75
Positive electrode	0.04
<i>Parameters</i>	
Emissivity	0.0
Volumetric heat capacity, $\text{J m}^{-3} \text{K}^{-1}$	2.14×10^6
$h, \text{W m}^{-2} \text{K}^{-1}$	20
a, m^{-1}	222
<i>Enthalpies of reactions</i>	
$H, \text{J g}^{-1}$	314
$H_1, \text{J g}^{-1}$	257
$H_2, \text{J g}^{-1}$	1714
<i>Frequency factors</i>	
A, min^{-1}	4×10^{13}
A_1, min^{-1}	1×10^{17}
A_2, min^{-1}	1.5×10^{15}
<i>Activation energies</i>	
$E_a/k_B, \text{K}$	14,738
$E_1/k_B, \text{K}$	16,246
$E_2/k_B, \text{K}$	16,246

List of symbols

a	active interfacial area per unit electrode volume, m^{-1}
A	cathode frequency factor, min^{-1}
A_1	anode SEI frequency factor, min^{-1}
A_2	anode intercalated lithium frequency factor, min^{-1}
Bi	Biot number
c_{elyte}	electrolyte concentration, mol m^{-3}
c_s	solid-phase Li concentration, mol m^{-3}
\tilde{C}_p	heat capacity, $\text{J kg}^{-1} \text{K}^{-1}$
D_{eff}	effective electrolyte diffusion coefficient, $\text{m}^2 \text{s}^{-1}$
D_s	solid-phase diffusion coefficient, $\text{m}^2 \text{s}^{-1}$
E_a	cathode decomposition activation energy, eV
E_1	anode SEI decomposition activation energy, eV
E_2	activation energy for anode intercalated lithium–electrolyte reaction, eV
F	Faraday's constant, $96,485 \text{C mol}^{-1}$
f_{+-}	mean molar activity coefficient
h	heat transfer coefficient, $\text{W m}^{-2} \text{K}^{-1}$
H	heat produced in cathode by the reaction per unit mass, J g^{-1}
H_1	heat produced in anode SEI by the reaction per unit mass, J g^{-1}
H_2	heat produced in intercalated lithium of anode by the reaction per unit mass, J g^{-1}
I	cell-sandwich current density, A m^{-2}
i_{elyte}	electrolyte-phase current density, A m^{-2}
i_n	transfer current per unit of interfacial area, A m^{-2}
i_0	exchange current density, A m^{-2}
j_n	normal molar flux, $\text{mol m}^{-2} \text{s}^{-1}$
k	thermal conductivity, $\text{W m}^{-1} \text{K}^{-1}$
k_B	Boltzmann constant, $8.617 \times 10^{-5} \text{ eV K}^{-1}$
L_c	characteristic length, m
n	number of electrons in redox reaction
\dot{q}	volumetric rate of heat generation, W m^{-3}
R	gas constant, $8.314 \text{ J mol}^{-1} \text{K}^{-1}$
s	stoichiometric coefficient of reactant
S_{abuse}	overall volumetric heat generation by abuse, W m^{-3}
S_{ne}	volumetric heat generation in the negative electrode due to thermal abuse, W m^{-3}
S_{pe}	volumetric heat generation in the positive electrode due to thermal abuse, W m^{-3}
S_{SEI}	volumetric heat generation in the SEI due to thermal abuse, W m^{-3}
t	time, s
T	temperature, K
t_+	cationic transference number
U_H	enthalpy potential, V
v	volume of jellyroll element, m^3
V	cell voltage, V
W	cell width, m
x_i	dimensionless amount of lithium intercalated within the carbon
x_f	dimensionless amount of lithium-containing metastable species in the SEI
α	fractional degree of conversion of cathode material during thermal abuse
α_a	anodic transfer coefficient
α_c	cathodic transfer coefficient

ε	porosity
Φ_{elyte}	electric potential in the solution, V
Φ_s	electric potential in the matrix, V
η_s	surface overpotential, V
κ	bulk electrolyte conductivity, S m^{-1}
ρ	density, kg m^{-3}
σ	matrix conductivity, S m^{-1}
ζ	dimensionless measure of the SEI thickness

References

- [1] T.M. Bandhauer, S. Garimella, T.F. Fuller, J. Electrochem. Soc. 158 (2011) R1–R25.
- [2] M. Fleckenstein, O. Bohlen, M.A. Roscher, B. Bäker, J. Power Sources 196 (2011) 4769–4778.
- [3] P. Ramadass, B. Haran, R. White, B.N. Popov, J. Power Sources 112 (2002) 606–613.
- [4] P. Ramadass, B. Haran, R. White, B.N. Popov, J. Power Sources 123 (2003) 230–240.
- [5] P. Liu, J. Wang, J. Hicks-Garner, E. Sherman, S. Soukiazian, M. Verbrugge, H. Tataria, J. Musser, P. Finamore, J. Electrochem. Soc. 157 (2010) A499–A507.
- [6] E.V. Thomas, H.L. Case, D.H. Doughty, R.G. Jungst, G. Nagasubramanian, E.P. Roth, J. Power Sources 124 (2003) 254–260.
- [7] K. Amine, J. Liu, I. Belharouak, Electrochim. Commun. 7 (2005) 669–673.
- [8] J.R. Belt, C.D. Ho, T.J. Miller, M.A. Habib, T.Q. Duong, J. Power Sources 142 (2005) 354–360.
- [9] J.R. Belt, C.D. Ho, C.G. Motloch, T.J. Miller, T.Q. Duong, J. Power Sources 123 (2003) 241–246.
- [10] I. Bloom, S.A. Jones, V.S. Battaglia, G.L. Henriksen, J.P. Christoffersen, R.B. Wright, C.D. Ho, J.R. Belt, C.G. Motloch, J. Power Sources 124 (2003) 538–550.
- [11] R. Wright, C. Motloch, J. Belt, J. Christoffersen, C. Ho, R. Richardson, I. Bloom, S. Jones, V. Battaglia, G. Henriksen, T. Unkelhaeuser, D. Ingersoll, H. Case, S. Rogers, R. Sutula, J. Power Sources 110 (2002) 445–470.
- [12] S. Peck, M. Pierce, in: SAE International, 2012. Warrendale, PA.
- [13] U.S. Kim, J. Yi, C.B. Shin, T. Han, S. Park, J. Electrochem. Soc. 158 (2011) A611–A618.
- [14] E. Barsoukov, J.H. Kim, C.O. Yoon, H. Lee, J. Power Sources 83 (1999) 61–70.
- [15] M.W. Verbrugge, R.S. Conell, J. Electrochem. Soc. 149 (2002) A45–A53.
- [16] J. Christensen, P. Albertus, D. Cook, in: Advanced Automotive Battery Conference, 2011. Pasadena, CA.
- [17] J. Christensen, D. Cook, P. Albertus, J. Electrochem. Soc. 160 (2013) A2258–A2267.
- [18] M. Doyle, T.F. Fuller, J. Newman, J. Electrochem. Soc. 140 (1993) 1526–1533.
- [19] T.F. Fuller, M. Doyle, J. Newman, J. Electrochem. Soc. 141 (1994) 982–990.
- [20] T.F. Fuller, M. Doyle, J. Newman, J. Electrochem. Soc. 141 (1994) 1–10.
- [21] D. Bernardi, E. Pawlikowski, J. Newman, J. Electrochem. Soc. 132 (1985) 5–12.
- [22] J. Christensen, P. Albertus, D. Cook, in: The Electrochemical Society Meeting 1622, 2011. Montreal, QC, Canada.
- [23] M.M. Thackeray, C. Wolverton, E.D. Isaacs, Energy Environ. Sci. 5 (2012) 7854–7863.
- [24] Available from: <http://www.teslamotors.com> (Accessed 03/31/14).
- [25] Available from: <http://www.gs-yuasa.com/us/>; <http://lithiumenergy.jp/en/products/index.html> (Accessed 03/31/14).
- [26] Available from: <http://www.ansys.com> (Accessed 03/31/14).
- [27] B.J. McBride, S. Gordon, and M.A. Reno, NASA October (1993) TM-4513.
- [28] J.W. Rose, J.R. Cooper, H.M. Spiers, Technical Data on Fuel, Wiley, New York, 1977.
- [29] W.C. Reynolds, Thermodynamic Properties in SI: Graphs, Tables, and Computational Equations for Forty Substances, Dept. Of Mechanical Engineering, Stanford University, Stanford, CA, 1979.
- [30] H. Maleki, S.A. Hallaj, J.R. Selman, R.B. Dinwiddie, H. Wang, J. Electrochem. Soc. 146 (1999) 947–954.
- [31] C. Peabody, C.B. Arnold, J. Power Sources 196 (2011) 8147–8153.
- [32] U.S. Kim, J. Yi, C.B. Shin, T. Han, S. Park, J. Power Sources 196 (2011) 5115–5121.
- [33] G.-H. Kim, K. Smith, K.-J. Lee, S. Santhanagopalan, A. Pesaran, J. Electrochem. Soc. 158 (2011) A955–A969.
- [34] S.J. Harris, A. Timmons, D.R. Baker, C. Monroe, Chem. Phys. Lett. 485 (2010) 265–274.
- [35] T.D. Hatchard, D.D. MacNeil, A. Basu, J.R. Dahn, J. Electrochem. Soc. 148 (2001) A755–A761.
- [36] M.N. Richard, J.R. Dahn, J. Electrochem. Soc. 146 (1999) 2078–2084.